Hannemann, K., Eulenfeld, T., Krüger, F., Dahm, T. (2022): Seismic scattering and absorption of oceanic lithospheric S waves in the Eastern North Atlantic. - Geophysical Journal International, 229, 2, 948-961.

https://doi.org/10.1093/gji/ggab493

Geophysical Journal International

Geophys. J. Int. (2022) **229,** 948–961
Advance Access publication 2021 December 04
GJI Seismology

https://doi.org/10.1093/gji/ggab493

Seismic scattering and absorption of oceanic lithospheric *S* waves in the Eastern North Atlantic

Katrin Hannemann,[1,2,*] Tom Eulenfeld,[3] Frank Krüger[1] and Torsten Dahm[1,4]

[1]*Institute of Geosciences, University of Potsdam,*14476 *Potsdam, Germany. E-mail: katrin.hannemann@uni-muenster.de*
[2]*Institute of Geophysics and Geology, University of Leipzig,* 04103 *Leipzig, Germany*
[3]*Institute of Geosciences, Friedrich Schiller University Jena,* 07749 *Jena, Germany*
[4]*Section* 2.1*, Physics of Earthquakes and Volcanoes, Helmholtz Centre Potsdam, GFZ German Research Centre for Geosciences,* 14473 *Potsdam, Germany*

Accepted 2021 December 2. Received 2021 November 30; in original form 2021 August 5

SUMMARY

The scattering and absorption of high-frequency seismic waves in the oceanic lithosphere is to date only poorly constrained by observations. Such estimates would not only improve our understanding of the propagation of seismic waves, but also unravel the small-scale nature of the lithosphere and its variability. Our study benefits from two exceptional situations: (1) we deployed over 10 months a mid-aperture seismological array in the central part of the Eastern North Atlantic in 5 km water depth and (2) we could observe in total 340 high-frequency (up to 30 Hz) *Po* and *So* arrivals with tens to hundreds of seconds long seismic coda from local and regional earthquakes in a wide range of backazimuths and epicentral distances up to 850 km with a travel path in the oceanic lithosphere. Moreover, the array was located about 100 km north of the Gloria fault, defining the plate boundary between the Eurasian and African plates at this location which also allows an investigation of the influence of an abrupt change in lithospheric age (20 Ma in this case) on seismic waves. The waves travel with velocities indicating upper-mantle material. We use *So* waves and their coda of pre-selected earthquakes to estimate frequency-dependent seismic scattering and intrinsic attenuation parameters. The estimated scattering attenuation coefficients are between 10^{-4} and 4×10^{-5} m^{-1} and are typical for the lithosphere or the upper mantle. Furthermore, the total quality factors for *So* waves below 5 Hz are between 20 and 500 and are well below estimates from previous modelling for observations in the Pacific Ocean. This implies that the Atlantic Ocean is more attenuative for *So* waves compared to the Pacific Ocean, which is inline with the expected behaviour for the lithospheric structures resulting from the slower spreading rates in the Atlantic Ocean. The results for the analysed events indicate that for frequencies above 3 Hz, intrinsic attenuation is equal to or slightly stronger than scattering attenuation and that the *So*-wave coda is weakly influenced by the oceanic crust. Both observations are in agreement with the proposed propagation mechanism of scattering in the oceanic mantle lithosphere. Furthermore, we observe an age dependence which shows that an increase in lithospheric age is associated with a decrease in attenuation. However, we also observe a trade-off of this age-dependent effect with either a change in lithospheric thickness or thermal variations, for example due to small-scale upwellings in the upper mantle in the southeast close to Madeira and the Canaries. Moreover, the influence of the nearby Gloria fault is visible in a reduction of the intrinsic attenuation below 3 Hz for estimates across the fault. This is the first study to estimate seismic scattering and absorption parameters of *So* waves for an area with several hundreds of kilometres radius centred in the Eastern North Atlantic and using them to characterize the nature of the oceanic lithosphere.

Key words: Body waves; Seismic attenuation; Wave scattering and diffraction.

*Now at: Institut für Geophysik, Westfälische Wilhelms-Universität Münster, 48149 Münster, Germany

1 INTRODUCTION

Since several decades, oceanic *Pn* and *Sn* waves—often referred to as *Po* and *So* waves—have been observed worldwide (Walker and Sutton 1971; Kennett *et al.* 2014; Krüger *et al.* 2020), but their properties and propagation have been seldom investigated and analysed in depth. These waves are reported to travel distances up to thousands of kilometres and show high-frequency (up to 30 Hz) *P*- and *S*-wave arrivals with tens to hundreds of seconds long seismic coda. Characteristic for these observations is the nearly instantaneously arriving energy on the radial and tangential components of recorded seismograms directly after the *P* onset on the vertical component, which implies an origin in a high scattering regime. On the other hand, *Po* and *So* waves show nearly equal amplitudes on all three components, which is indicative for a nearly horizontal wave propagation. Several authors (Kennett & Furumura 2013; Shito *et al.* 2013; Kennett *et al.* 2014; Shito *et al.* 2015) showed that these waves can be modelled if a heterogeneous oceanic lithosphere is assumed. The heterogeneous models often consist of isotropic material that has a much longer horizontal than vertical correlation length and is therefore quasi-laminar and behaves anisotropic (Kennett *et al.* 2014). Moreover, Kennett *et al.* (2014) found that the diffuse wavefield is rather robust to any disturbance once it has been established—especially in thicker lithosphere, as it is self healing and resilient to changes in wave speed structure due to its diffuse character. Even the transition between two lithospheric segments with different thickness or the passage of a fracture zone cannot suppress *Po* or *So*, but only reduces their amplitude due to local energy loss (Kennett *et al.* 2014). However, Kennett & Furumura (2013) demonstrated that *Po* and *So* waves are still sensitive to changes in attenuation, for example as introduced by thermal variation. The thermal state has a dominant influence on intrinsic attenuation and is more important than the oceanic age for high-frequency propagation in case of thermal variations such as the influence of hotspots (Jackson 2007; Kennett *et al.* 2014). In their modelling Kennett *et al.* (2014) also showed the trade-off between the quality factor for *S* waves (Q_s) and the thickness of the lithosphere, demonstrating that reducing lithospheric Q_s has a similar effect on the propagated wavefield as reducing the thickness of the lithosphere. The authors also concluded that *So* is more sensitive to effects of lateral variations of lithospheric structure and seismic attenuation. However, it has to be noted that the numerical models are so far limited to waves with frequencies below 5 Hz (Shito *et al.* 2013, 2015) or 10 Hz (Kennett & Furumura 2013; Kennett *et al.* 2014) and often assume frequency independent attenuation parameters and only allow a qualitative estimate of attenuation parameters.

In this study, we focus on the Eastern North Atlantic in the greater vicinity of the Gloria fault (Fig. 1a) that is a major transform fault and part of the Eurasian–African plate boundary. This plate boundary is suspected to have hosted the 1755 earthquake that caused a major tsunami being responsible for major destruction in Lisbon (Vilanova *et al.* 2003). Furthermore, the region is influenced by two known hotspots close to the Azores and the Canary Islands (Fig. 1a). The locations of the hotspots have been mapped by identifying depressions in the topography of the 410 km discontinuity, which indicate elevated temperatures (Saki *et al.* 2015). We use a seismological array that was installed from July 2011 until April 2012 in 5000 m water depth about 100 km north of the Gloria fault. Within this 10 months' period, Krüger *et al.* (2020) identified 349 local and regional earthquakes for epicentral distances up to 850 km (Fig. 1a) by using incoherent beamforming. The acquired earthquake recordings show high-frequency (up to 30 Hz) *P*- and *S*-wave arrivals with tens to hundreds of seconds long seismic coda (Fig. 2). They show the typical appearance of *Po* and *So* waves with the dominant energy in the first 30 s and a gentle decay into an elongated coda afterwards as described by Kennett *et al.* (2014). Furthermore, the observed high-frequency content and the increase of its relative portion in later coda wave time windows (Fig. 2) have also been reported for other studies (Walker & Sutton 1971; Kennett *et al.* 2014). The waves travel with velocities that are characteristic for upper-mantle material. One major difference of this study to previous *Po* and *So* studies focusing mainly on the Pacific Ocean is the slower spreading rate of the Atlantic Ocean (1–3 cm a^{-1}, Müller *et al.* 2008). Kennett *et al.* (2014) expected that due to the slower spreading rates, the horizontal and vertical correlation lengths tend to be more similar. This near isotropic heterogeneity will still produce high-frequency guided waves, but the generated stochastic wavefield will be less stable and would not be sustainable for very long distances and more sensible to changes in lithospheric properties, such as thickness and attenuation (Kennett *et al.* 2014).

In the following, we estimate frequency-dependent seismic scattering and intrinsic attenuation parameters based on envelope modelling of *So* waves and their codas. The analysis is done for different azimuth bins, in order to allow a comparison for different ocean ages and lithospheric thicknesses. This allows to characterize the attenuation of *So* waves in the Eastern North Atlantic and gives implication on the overall oceanic lithospheric structure in this region. Furthermore, as we also record *So* waves that travelled across the Gloria fault, the influence of the fault on the attenuation is analysed. Finally, we use the obtained results to characterize the thermal state of the oceanic lithosphere in different azimuthal ranges.

2 DATA

We use data recorded on a 75 km aperture ocean bottom array that was located approximately 100 km north of the Gloria fault in the deep ocean (approx. 5000 m water depth) about 800 km from Portugal mainland and also from the Azores (Fig. 1a). The data have been recorded at 11 free fall ocean bottom stations (OBSs; Fig. 1b) from DEPAS (Deutscher Geräte-Pool für amphibische Seismologie/German instrument pool for amphibian seismology). Each station was equipped with a wide band Guralp CMG 40 T (60 s eigenperiod) three-component sensor, a broad-band hydrophone (HTI-04-PCA/ULF) and a Send Geolon MCS recorder (Stähler *et al.* 2016; Alfred-Wegener-Institut Helmholtz-Zentrum für Polar- und Meeresforschung *et al.* 2017). The data were recorded with a sampling frequency of 100 Hz. The recording period was 10 months (June 2011 until April 2012). The data have been corrected for clock drifts and static time-shifts (Hannemann *et al.* 2014) and the orientation of the horizontal seismometer components were estimated using the particle motion of *P* waves and Rayleigh waves of teleseismic earthquakes (Hannemann *et al.* 2017). Furthermore, an incoherent beamforming approach has been used to search the continuous data for local and regional (up to 850 km epicentral distance) earthquakes mainly in the oceanic parts of the Eurasian and African plates (see yellow and orange circles in Fig. 1a and Krüger *et al.* 2020 for processing details). The final earthquake catalogue contains 349 events. The majority of these events are located along the plate boundary, in addition several small spatial clusters are located towards the north

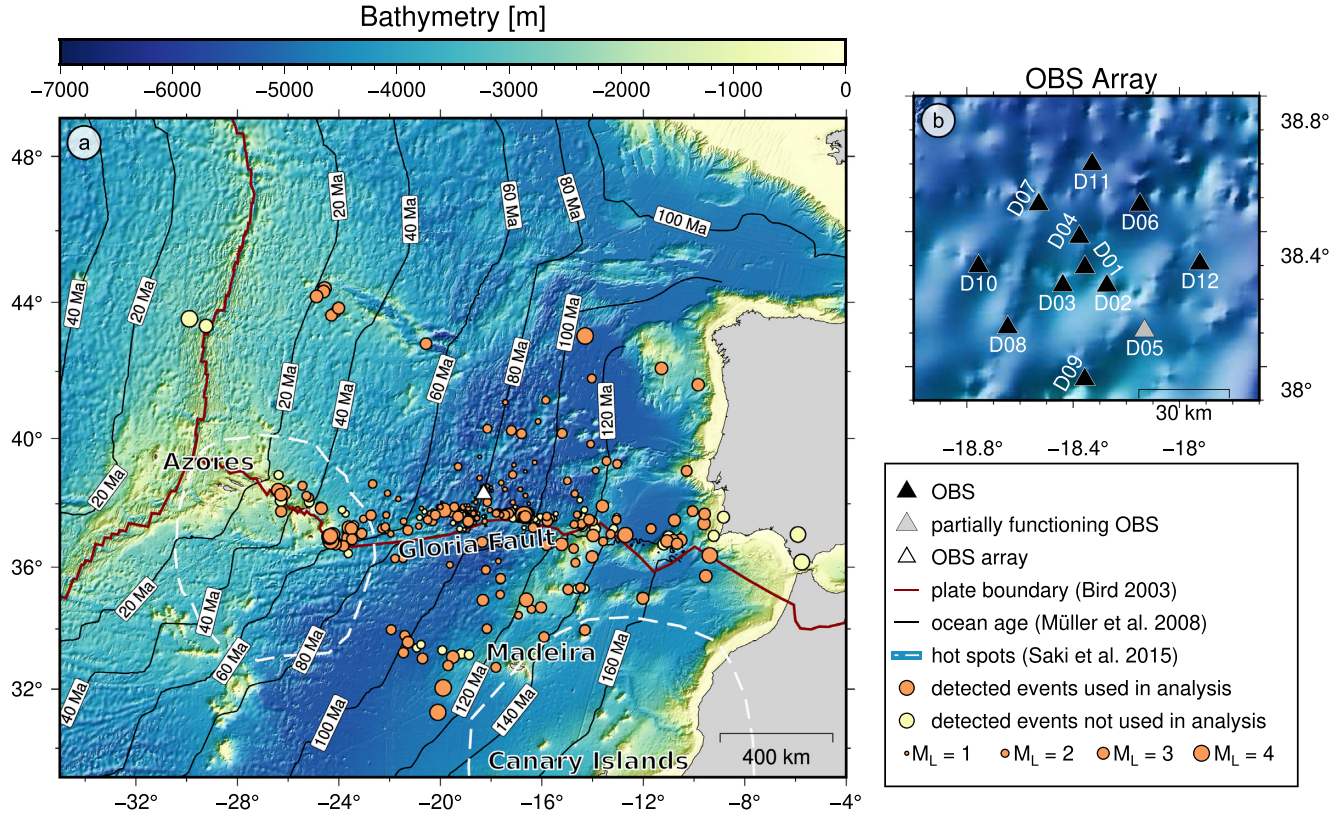

Figure 1. (a) Bathymetric map of the Eastern North Atlantic (GEBCO Compilation Group 2020) showing the distribution of earthquakes (light yellow and orange circles) detected by the OBS array (white triangle). Only events shown as orange circles were used for the analysis. Furthermore, the lithospheric ages (Müller *et al.* 2008) are shown as contours, plate boundaries as thick red lines (Bird 2003) and the approximate location of hotspots in this area by white dashed lines (Saki *et al.* 2015). (b) Layout of the OBS array. The station shown in grey had clamped components and was therefore not used in the analysis.

and south of the array and seem to be associated with morphological features also visible in the bathymetry (Fig. 1a). These local and regional events show the typical characteristics of *Po* and *So* waves (Fig. 2).

Krüger *et al.* (2020) observed that the *Po* and *So* waves travel with typical upper-mantle velocities, which agrees with the hypothesis that these waves mainly propagate in the oceanic mantle lithosphere. The amplitudes of the *Po* and *So* waves are quite similar on all three components that are inline with the proposed propagation mechanism through scattering. The coda lasts for more than 100 s, is diffuse and has energy at frequencies up to 30 Hz and sometimes also higher (Fig. 2b) on all three components.

3 ESTIMATION OF ABSORPTION AND SCATTERING

In the following analysis we focus on the *So* wave and its coda. We exclude the *Po* wave as its coda might be influenced by the later arriving *So* wave. Furthermore, simulations (Kennett & Furumura 2013; Kennett *et al.* 2014) indicate that the *So* wave is more sensitive to changes in lithospheric properties (e.g. thickness and attenuation) than the *Po* wave. The python toolbox *Qopen* (Eulenfeld & Wegler 2016) allows the simultaneous determination of intrinsic and scattering attenuation parameters by envelope inversion of the recorded *So* wave. For the analysis, we calculate the energy density of the waveform recordings for a combination of all three components for different frequency bands by

$$E_{\mathrm{obs}}(t, \mathbf{r}) = \frac{\rho_0 \langle \dot{u}(t, \mathbf{r})^2 \rangle}{C \Delta f} \tag{1}$$

in which ρ_0 is the mean mass density and $\langle \dot{u}(t, \mathbf{r})^2 \rangle$ is the mean square velocity, that is the envelope of the recorded *So* wave. The normalization factor Δf describes the width of the used filter (Eulenfeld & Wegler 2016). The factor C is a projection factor (Emoto *et al.* 2010) that corrects the influence of the amplification of an incident wave (e.g. by the free surface) on the estimated energy value. As we are analysing *So*-wave data from the ocean bottom, we have to re-evaluate this factor to check whether it is feasible to apply $C = 4$, as it would be done in case of the free surface (Eulenfeld & Wegler 2016). The factor C should correct for the amplification at the interface between ocean bottom and water column, therefore it is valid to consider an isotropic medium above and below this interface and to separately evaluate the case of an incident horizontally polarized S wave (*SH* wave) and an incident vertically polarized S wave (*SV* wave). In the *SH* wave case, the wave energy is totally reflected and the resulting amplification is 4 and is independent of the incidence angle. For the *SV* wave case, we find that the amplification at the ocean bottom is comparable to the free surface case (Fig. 3, for further details see the Appendix) and at least for small incidence angles ($<30°$) $C = 4$ is valid.

Kennett & Furumura (2013) showed that the *So* waves propagate nearly horizontally through the oceanic lithosphere. We therefore use the analytical approximation of 2-D isotropic radiative transfer (Paasschens 1997) as Green's function to model the direct and the

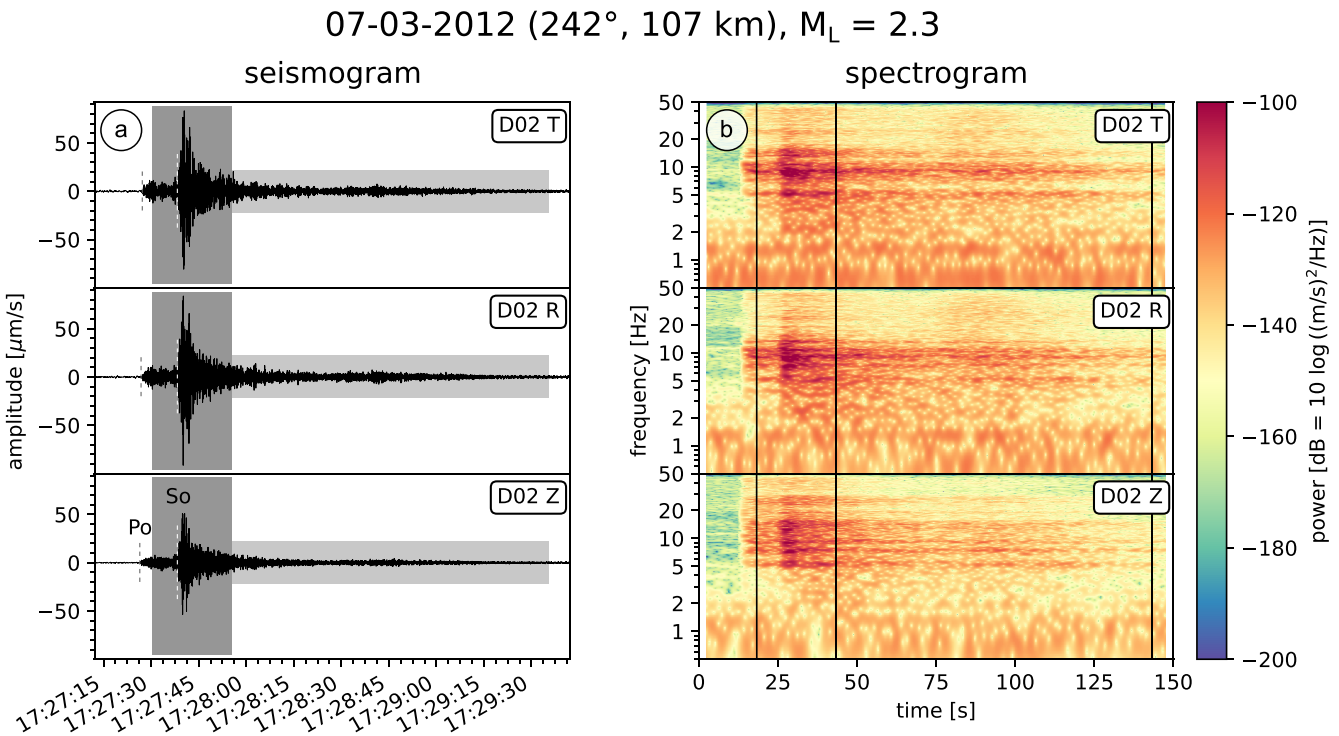

Figure 2. (a) Example for three-component seismogram showing a regional event (2012 March 7, 107 km epicentral distance, 242° backazimuth, M_L 2.3) with characteristic *Po* and *So* waves. The data were high pass filtered at 0.88 Hz. The dark grey shaded areas mark the chosen time window for estimating the mean amplitude of the direct *S* wave and the light grey shaded areas mark the chosen coda wave time window. The dark grey dashed line marks the *Po*-wave onset and the white dashed line the *So*-wave onset. (b) Spectrograms for all three components of same event as presented in (a). The lines mark the chosen time windows for direct *S* wave and coda wave.

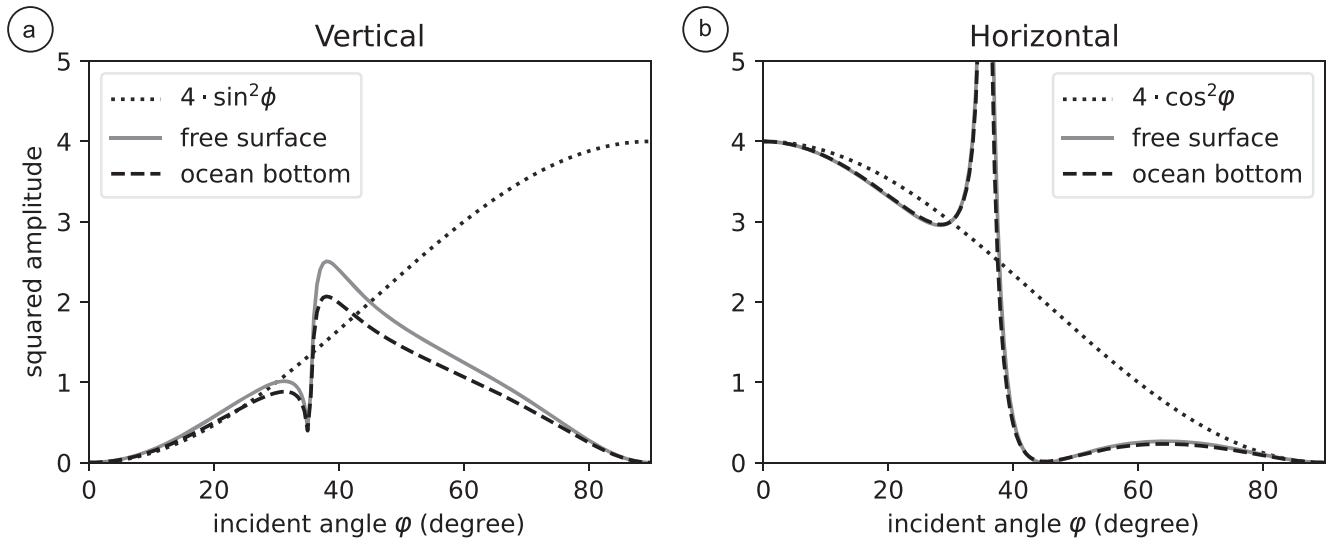

Figure 3. Comparison of amplification factors at the free surface (grey solid line) and the ocean bottom (black dashed line) for an incident *SV* wave for a medium with $v_p/v_s = \sqrt{3}$ in comparison to four times the projection factor (dark grey dotted line). (a) Vertical amplification. (b) Horizontal amplification. Modified after Emoto *et al.* (2010, fig. 8).

scattered wavefield:

$$G_{2D}(t, r, g_0) = \underbrace{e^{-v_s t\, g_0}\, \frac{\delta(r - v_s t)}{2\pi v_s t}}_{\text{direct wave}} + \underbrace{\frac{g_0}{2\pi v_s t}\, \frac{1}{\sqrt{1 - \frac{r^2}{v_s^2 t^2}}}\, e^{g_0\left(\sqrt{v_s^2 t^2 - r^2} - v_s t\right)} \Theta(v_s t - r)}_{\text{scattered wave}}. \quad (2)$$

The Green's function depends on the time t, the distance r between source and receiver and the transport scattering coefficient g_0. The mean S wave velocity v_s is assumed to be constant along the whole ray path. In contrast to the 3-D Green's function used by Eulenfeld & Wegler (2016), the 2-D Green's function has the dimension m^{-2} instead of m^{-3}, we therefore have to normalize the resulting energy by the inverse of the median lithospheric thickness along the ray path ($\tilde{D}_L$) to properly model the energy of the wave:

$$E_{mod}(t, r) = \frac{W\, R(r)}{\tilde{D}_L}\, G_{2D}(t, r, g_0)\, e^{-bt}. \quad (3)$$

Herein, e^{-bt} describes the exponential decrease due to intrinsic attenuation, which is described by the intrinsic attenuation coefficient b. The spectral source energy W and the energy site amplification factor R account for the influences of the source and the receiver site (Eulenfeld & Wegler 2016). These two parameters will not be analysed in this study.

Justified by recent studies (Hannemann *et al.* 2016; Krüger *et al.* 2020), we use a mean S-wave velocity of 4600 m s^{-1}. This velocity gives a good match of the *So*-wave arrival for a wide distance range (Fig. 4). Furthermore, we choose a mean mass density of 3380 g m^{-3} that corresponds to the density given for the lithospheric mantle by PREM (Dziewonski & Anderson 1981). We filter the data with different second-order, zero-phase Butterworth filters in octave frequency bands with centre frequencies between 1 and 30 Hz, resulting in nine analysed frequency bands. In order to correct for the noise level, we use the minimum average amplitude of five 10-s-long noise time windows (see Table 1 for times) for the correction of the energy envelope. The bulk time window for the *So* wave and the coda time window is chosen relative to the *S* onset (see Table 1). For the inversion, the data in the coda time window is smoothed in 5 s Bartlett time windows. Furthermore, we shorten the coda-time window either if the signal-to-noise ratio (SNR) drops below 2 or at a local minimum if this minimum is followed by a local maximum with twice the amplitude of the minimum. The SNR is determined by using the minimum average amplitude of the noise time windows and the energy density of the wave form recordings (eq. 1). The shorting of the coda-time window in case of a local minimum is done to exclude additional phases that may arrive later in the *S*-wave coda. The inversion is not done if the coda time window is shorter than 10 s and if there are less than two station–event pairs left after the exclusion of data.

The modelling by Kennett & Furumura (2013) showed that *So* waves are sensitive to lateral variations in lithospheric structure and seismic attenuation, therefore we decided to analyse the regional events in 45° azimuth bins each 15° to obtain more stable results that can also be compared with the age and thickness of the lithosphere. A look at the azimuthal distribution for the 45° bins each 15° (Fig. 5a) shows that most of the events are located in the azimuthal bins around 120° and 240°. This corresponds to the azimuthal directions of the plate boundary (compare Fig. 1a). Moreover, a horse shoe like pattern is observable in the azimuth–distance distribution (Fig. 5c), which can be associated with the plate boundary. In order to obtain comparable results for the simultaneously inverted events for each azimuth bin, we decided to further subdivide the events in each azimuth bin in 50 km distance bins and choose only the two to three strongest events in each azimuth–distance bin (Fig. 5d). For all results presented in this study, we simultaneously analyse the recordings at all stations of the array. However, the applied quality criteria mentioned before may lead to an exclusion of specific station–event pairs from the analysis; therefore, not all events are inverted for all stations.

For better comparability with other studies, we calculate inverse quality factors for intrinsic (Q_i^{-1}), scattering (Q_{sc}^{-1}) and total attenuation (Q_{tot}^{-1}) from the obtained attenuation coefficients (g_0 and b):

$$Q_i^{-1} = \frac{b}{2\pi f}, \quad (4)$$

$$Q_{sc}^{-1} = \frac{g_0 v_s}{2\pi f}, \quad (5)$$

$$Q_{tot}^{-1} = Q_i^{-1} + Q_{sc}^{-1}. \quad (6)$$

Furthermore, we estimate the seismic albedo B_0, which indicates whether the scattering or intrinsic attenuation dominates the total attenuation:

$$B_0 = \frac{Q_{sc}^{-1}}{Q_{tot}^{-1}}. \quad (7)$$

Finally, we also calculate the absorption and transport mean free path length (l_i and l_{sc}) whose values can indicate the length scale of the most relevant structures for the propagation of the waves (Sato *et al.* 2012):

$$l_i^{-1} = \frac{v_s}{b}, \quad (8)$$

$$l_{sc}^{-1} = \frac{1}{g_0}. \quad (9)$$

4 RESULTS

In Fig. 6(a), we show an exemplary comparison of the recorded waveform energy and the modelled energy for the different frequency bands between 0.8 and 40 Hz. As can be seen, the modelled energy fits well to the recorded energy for frequencies above 2 Hz. Furthermore, we present the estimates for the transport scattering coefficient g_0 (Fig. 6b) and intrinsic attenuation coefficient b (Fig. 6c) with frequency for all azimuth bins and for the azimuth bin between 240° and 285°, in which the event shown in Fig. 6(a) lies. The frequencies in Figs 6(b) and (c) correspond to the centre frequency of the frequency bands named in Fig. 6(a). As already mentioned in the previous section, recordings of the coda wave were shortened if the SNR drops below 2 or if a local maximum is present and furthermore too short coda time windows (<10 s) were removed during the inversion. We therefore grouped the presented results based on the number of finally used events (indicated by transparency in Figs 6b and c) to indicate the quality of the estimates.

In general, the transport scattering coefficient g_0 is decreasing for higher frequencies except for the last frequency band (20–40 Hz) for which a small increase is visible. The g_0 values range between 10^{-4} and 4×10^{-5} m^{-1}. For the intrinsic attenuation coefficient b, we estimated nearly constant values between 3×10^{-2} and 5×10^{-2} s^{-1} for centre frequencies between 2 and 10 Hz.

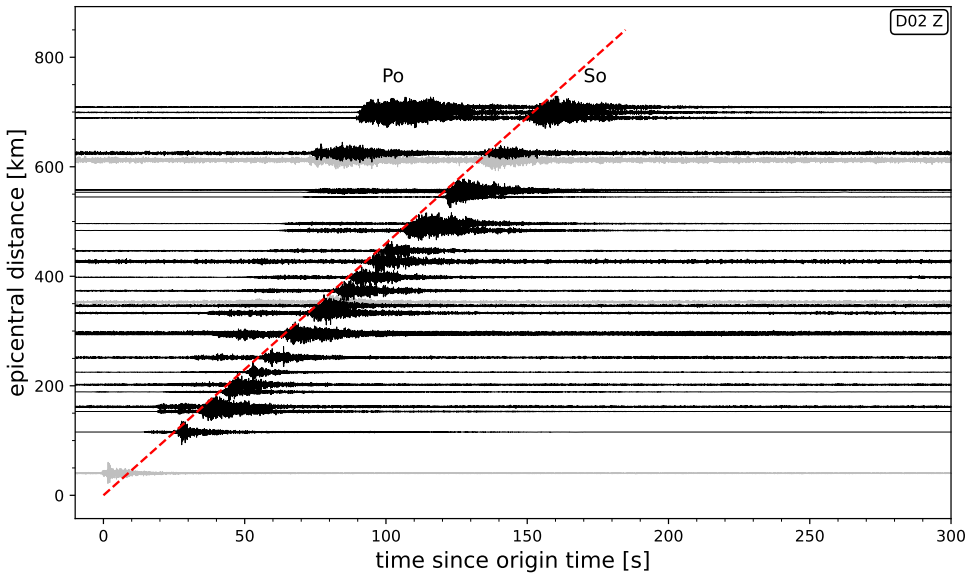

Figure 4. Recordings of vertical component of Station D02 for all events that have been analysed for the azimuth bin between 240° and 285°. The light grey traces show those events that have been excluded from the analysis for station D02 due to the quality criteria. The dashed red line corresponds to a velocity of 4600 m s^{-1}. The time is given relative the origin time of each event.

Table 1. Time windows used for inversion with *Qopen*. List of used abbreviations: OT = origin time; ST = *S*-onset time.

Type	Start	EndN
Noise time window 1	OT-20 s	OT-10 s
Noise time window 2	OT-10 s	OT
Noise time window 3	OT	OT+10 s
Noise time window 4	OT+10 s	OT+20 s
Noise time window 5	OT+20 s	OT+30 s
Bulk time window	ST-5 s	ST+20 s
Coda time window	ST+20 s	ST+120 s

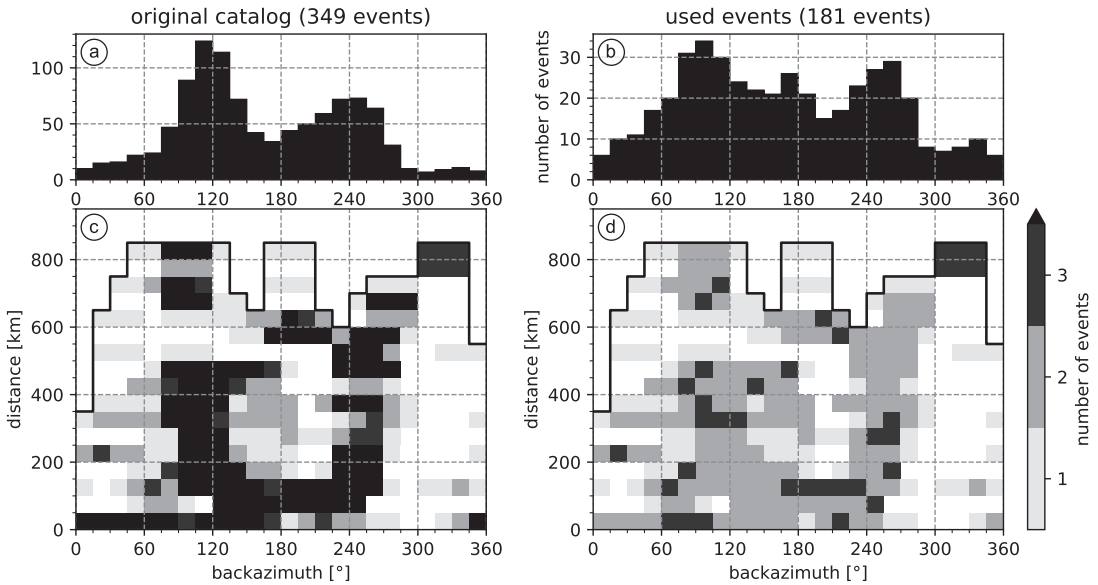

Figure 5. Azimuth–distance distribution of used events. We analyse the events in 45° wide azimuth bins every 15° up to a epicentral distance of 850 km. (a) Number of events per azimuth bin for all events in original catalogue up to an epicentral distance of 850 km. (b) Number of events per azimuth bin which have been simultaneously inverted. (c) Number of events per azimuth and 50 km distance bin in original catalogue up to an epicentral distance of 850 km. (d) Number of simultaneously inverted events per azimuth and 50 km distance bin.

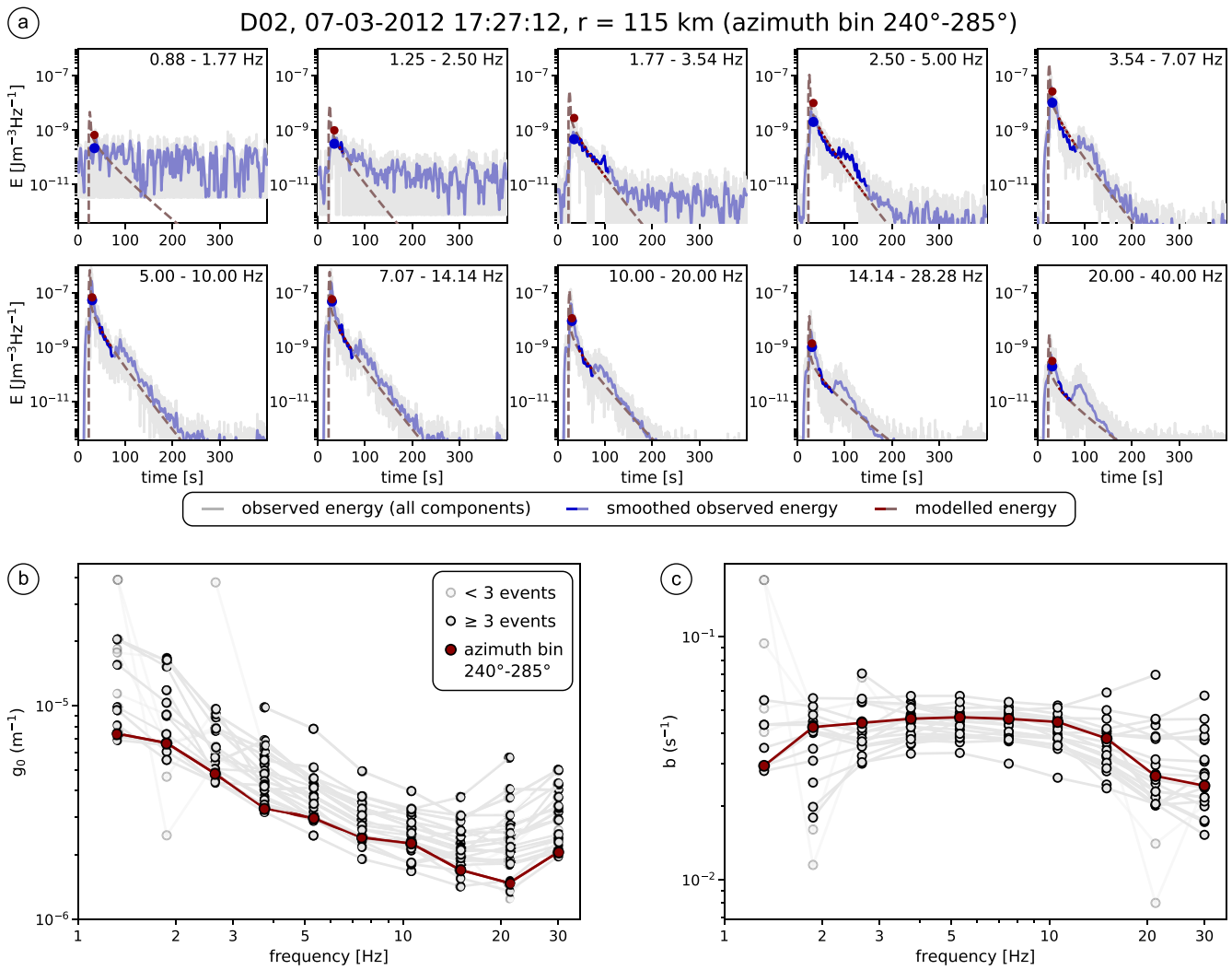

Figure 6. (a) Comparison between observed (grey), smoothed observed (blue) and modelled (dashed red) energy densities at station D02 for event shown in Fig. 2 in all frequency bands used in the analysis. For the modelled energy, the transport scattering and intrinsic attenuation coefficients estimated for the azimuth bin 245–285° were used. The averaged *So*-wave amplitude of the bulk time window is marked as a dot for the observed (blue) and the modelled (red) energies. The used coda wave time windows are presented in darker colours. Estimated (b) transport scattering coefficient g_0 and (c) intrinsic attenuation coefficient b for different frequencies in the azimuth bin between 240° and 285° (red curve) and all other azimuth bins (grey curves). Transparency indicates the number of events used for the analysis.

For the comparison of the attenuation parameters with lithospheric age and thickness, we used the ocean ages provided by Müller *et al.* (2008) and extracted lithospheric thicknesses from the LITHO1.0 model (Pasyanos *et al.* 2014) which employs surface wave modelling. The latter was done by extracting the top of the uppermost sedimentary or crustal layer and the bottom of the lithospheric mantle for 0.2° steps in latitude and longitude (Fig. 7). Up to an age of 80 Ma, there seems to be a direct correlation between lithospheric thickness and ocean age. This is mainly true for areas west of the OBS array (Fig. 7). In the east, we see a greater variation in lithospheric thickness which shows no direct correlation with ocean age (Fig. 7). Based on these observations, we decided to analyse the obtained attenuation results as a function of azimuth and not directly as a function of ocean age or lithospheric thickness, as we think that neither the ocean age nor the lithospheric thickness can solely be used to interpret the obtained results. We estimated the median ocean age and lithospheric thickness for every 45° azimuth bin every 15° and the further subdivisions in the 50 km distance bins (Fig. 8).

In Fig. 8, we present the obtained inverse quality factors for intrinsic (Fig. 8a) and scattering (Fig. 8b) attenuation for different frequencies, as well as the median age (Fig. 8c) and median lithospheric thickness (Fig. 8d) for different distance ranges. In order to facilitate interpretation, we subdivided the data in four azimuthal ranges: north (300–60°), south (120–240°), west (210–330°) and east (30–150°). The results of the north and south ranges are presented from west to east and the results of the west and east range from north to south. The overlaps of 30° between neighbouring azimuthal ranges should help to identify trends with backazimuth in the presented results. Overall, the inverse quality factors decrease with increasing frequency for all azimuth bins. However, there are slight changes for different azimuths in the inverse quality factors.

For the north, the inverse quality factor for intrinsic attenuation (Q_i^{-1}, Fig. 8a) ranges between 1.4×10^{-4} and 3.2×10^{-3} if at least the recordings of three events are included in the inversion ($6.0 \times$

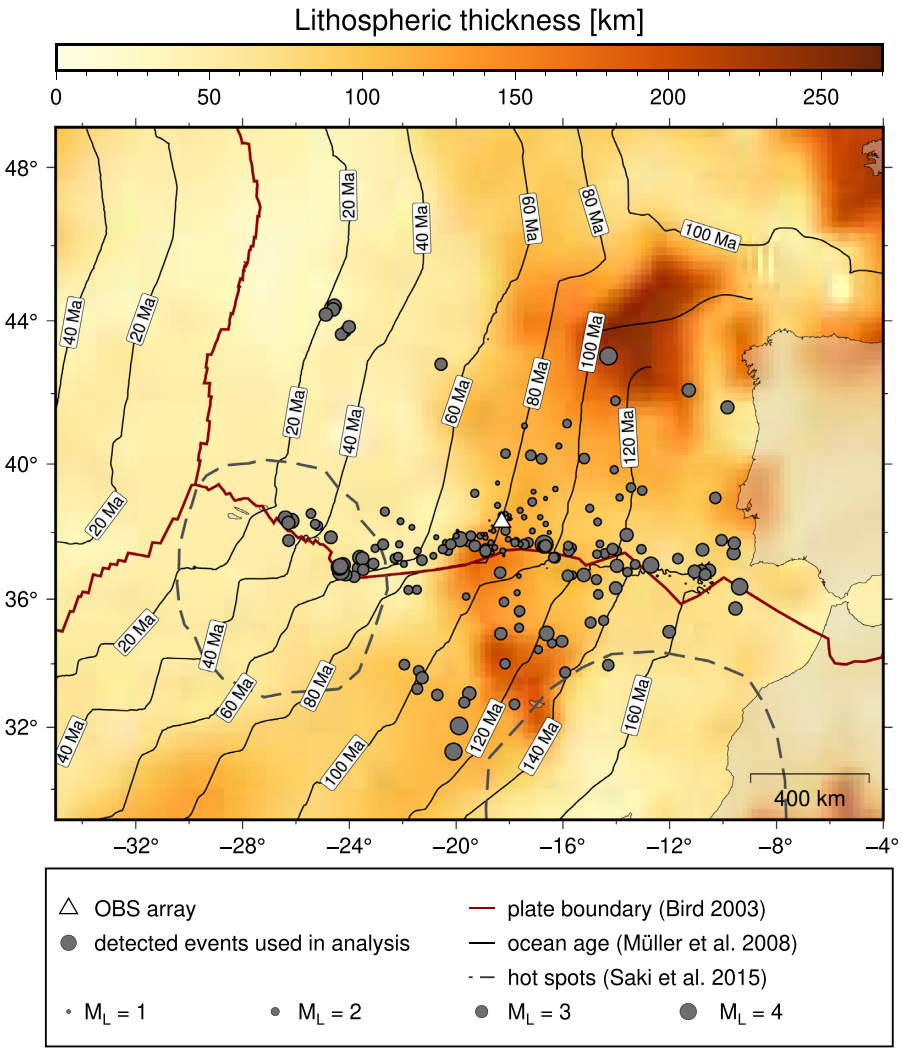

Figure 7. Lithospheric thickness as extracted from the LITHO1.0 model (Pasyanos *et al.* 2014). In addition, the used events (selected from the catalogue by Krüger *et al.* 2020), the ocean ages (Müller *et al.* 2008), plate boundaries (Bird 2003) and locations of known hotspots (Saki *et al.* 2015) are shown.

10^{-5} to 2.0×10^{-2}, if results obtained with less than three events are additionally taken into account) and shows a slight increase from west to east in all frequencies for results obtained with at least three events. The southern azimuths show a wider range from 9.2×10^{-5} to 5.2×10^{-3} (9.2×10^{-5} to 5.2×10^{-3}) and a small undulation from west to east which peaks around 175°. For the west, we obtained Q_i^{-1} values between 1.1×10^{-4} and 4.7×10^{-3} (6.0×10^{-5} to 6.1×10^{-3}) which show an undulation which peaks around 295°. The eastern azimuths show a decrease from north to south and Q_i^{-1} ranges between 8.1×10^{-5} and 6.6×10^{-3} (8.1×10^{-5} to 2.1×10^{-2}).

The inverse quality factor for scattering attenuation (Q_{sc}^{-1}, Fig. 8b) ranges between 7.2×10^{-5} and 2.2×10^{-3} (4.3×10^{-5} to 2.1×10^{-2}) for northern azimuths. Similar to the inverse quality factor for intrinsic attenuation, it shows a slight increase from west to east. In the south, the estimated Q_{sc}^{-1} values are between 5.2×10^{-5} and 1.1×10^{-2} (5.2×10^{-5} to 1.1×10^{-2}). The values show a small undulation with backazimuth and peak around 215° and 155°. For western azimuths, Q_{sc}^{-1} values undulates between 4.7×10^{-5} and 6.4×10^{-3} (4.3×10^{-5} to 6.4×10^{-3}). The values peak around 295° and increase from 235° towards 215°. In the east, we again observe a similar behaviour of Q_{sc}^{-1} as for Q_i^{-1} with a slight decrease from north to south. The Q_{sc}^{-1} values lay between 5.0×10^{-5} and 2.1×10^{-2}.

The ocean ages (Fig. 8c) show a clear pattern for the four azimuthal ranges. For all azimuth bins we observe a clear trend in age with increasing distance from the array, getting either younger or older. In the north, we observe an increase in age from 10–80 to 80–130 Ma going from west to east, as we would expect it from the map in Fig. 1. Furthermore, in the south we also observe an increase from 45 to 100 Ma in the west to 80–180 Ma in the east. In addition, a gap of approximately 20 Ma is visible for the distance bins below and above 100–200 km which corresponds to the age difference across the Gloria fault. Moreover, western azimuths have the youngest ocean ages and are nearly constant between 10 and 80 Ma for azimuths between 260° and 330°. They increase towards the south reaching values between 60 and 120 Ma. The eastern azimuths have the oldest ages, between 30° and 80° they are nearly constant between 70 and 130 Ma and increase for the azimuths between 80° and 150° to ages between 80 and 180 Ma.

In addition, it becomes clear that the lithospheric thicknesses (Fig. 8d) overall show no correlation with the ocean ages. For all azimuth ranges, they do not show a clear distance dependency. For northern azimuths, the median lithospheric thickness first increases

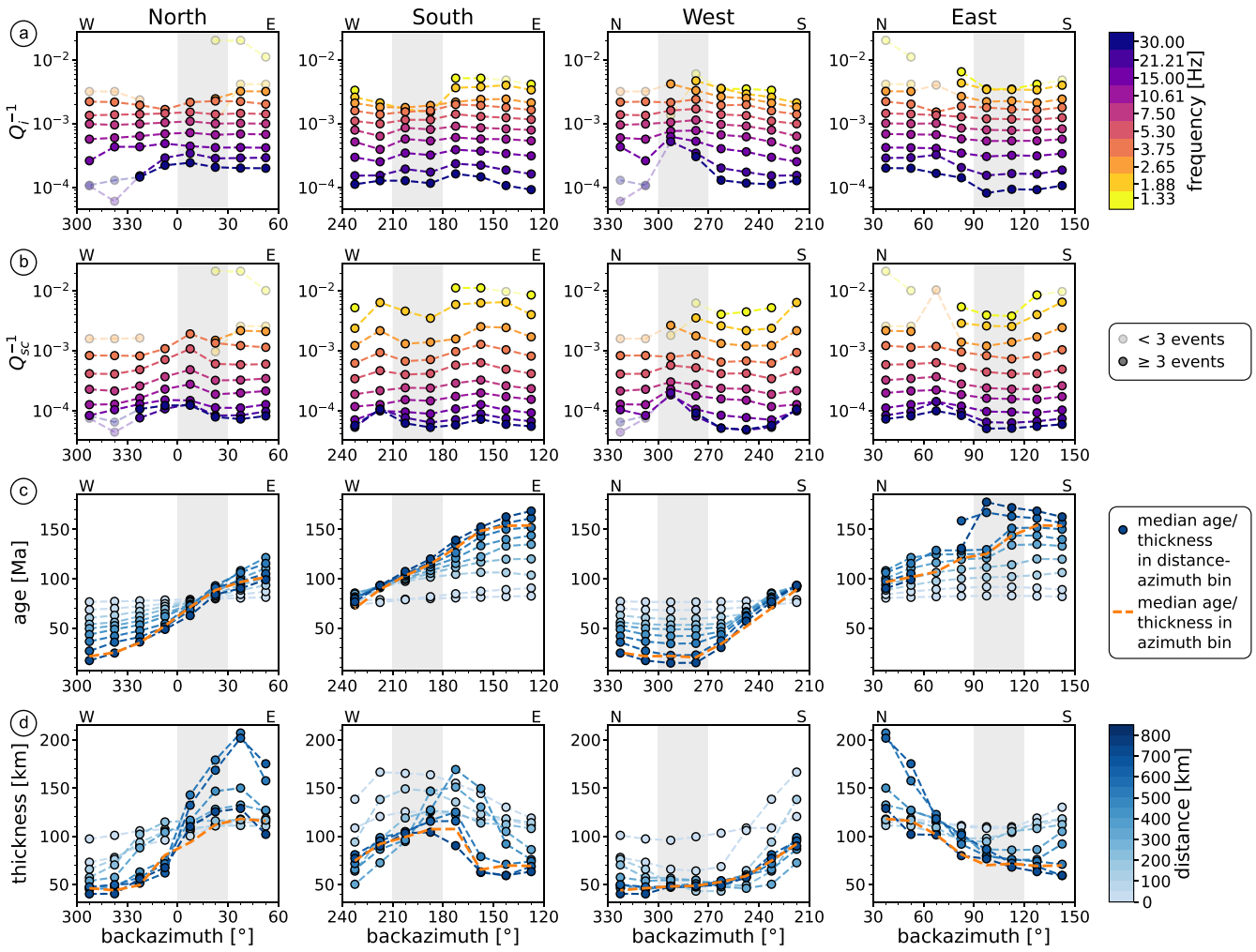

Figure 8. Estimated inverse quality factors for (a) intrinsic (Q_i^{-1}) and (b) scattering (Q_{sc}^{-1}) attenuation for different frequencies in each azimuthal bin and (c) extracted median age (Müller *et al.* 2008), as well as (d) median lithospheric thickness (Pasyanos *et al.* 2014) for each azimuth–distance bin (circles) and for each azimuth bin (orange dashed lines). Grey shaded areas mark data presented in Fig. 9. Transparency indicates number of used events. Note that the backazimuth axis of the southern and western azimuths are flipped for better comparability with northern and eastern azimuths. The colours in (a) and (b) indicate the centre frequency of the applied frequency band. In (c) and (d), the colours show the distance from the array for the corresponding azimuth–distance bin.

starting between 40 and 100 km in the west and reaching thicknesses of 100–200 km at around 45° and then slightly decreases to 100–180 km towards the east. In the southern azimuthal range, they increase from 50 to 140 km in the west to 100–160 km between 180° and 210° and decrease to 60–130 km in the east. For western azimuths, we observe nearly constant thickness between 40 and 100 km from 260° to 330° and an increase to 60–160 km towards the south. The eastern azimuth bins show a decrease from north to south from 110–210 km towards 50–140 km.

Another way to look at the dependency of the attenuation on ocean age and lithospheric thickness is to focus on those azimuth bins with the youngest and oldest ocean ages in the west and east. Perpendicular to these two directions one can focus on the azimuth bins with nearly the smallest variation in age towards the north and the azimuth bins with the clearest age gap towards the south (grey shaded areas in Fig. 8). We present the selected curves as function of distance and frequency respectively in Fig. 9.

As can be seen in Fig. 9(a), the ages close to the array are comparable for all four directions but for greater distances, the age differences become clearer. The youngest ages are found towards the west. In the north, we have nearly constant ages with distance. Similar is true for the south, except for a jump of about 20 Ma at a distance of around 175 km. The oldest ages are found towards the east. In Fig. 9(b), we see that the inverse quality factor for intrinsic attenuation decreases nearly linearly with frequency in the log–log graph for all four azimuthal ranges. For frequencies above 3 Hz the inverse quality factor is decreasing from west to north to south to east. For the scattering attenuation (Fig. 9c), the decrease with frequency is similar. For frequencies above 3 Hz, the curves for eastern and southern azimuths are quite similar, western and northern azimuths show slightly higher values. If we look at the inverse quality factor for the total attenuation (Fig. 9d), we again observe a linear decrease with frequency in the log–log graph and for frequencies above 10 Hz a decrease in the inverse quality factor from west to north to south to east, but not as clear as in case of the intrinsic attenuation.

The lithospheric thicknesses for the four azimuthal ranges (Fig. 9e) show much more variation with distance than the ages. For western azimuths, we observe a decrease in thickness up to a distance of around 200 km from 100 to 50 km, for larger distances

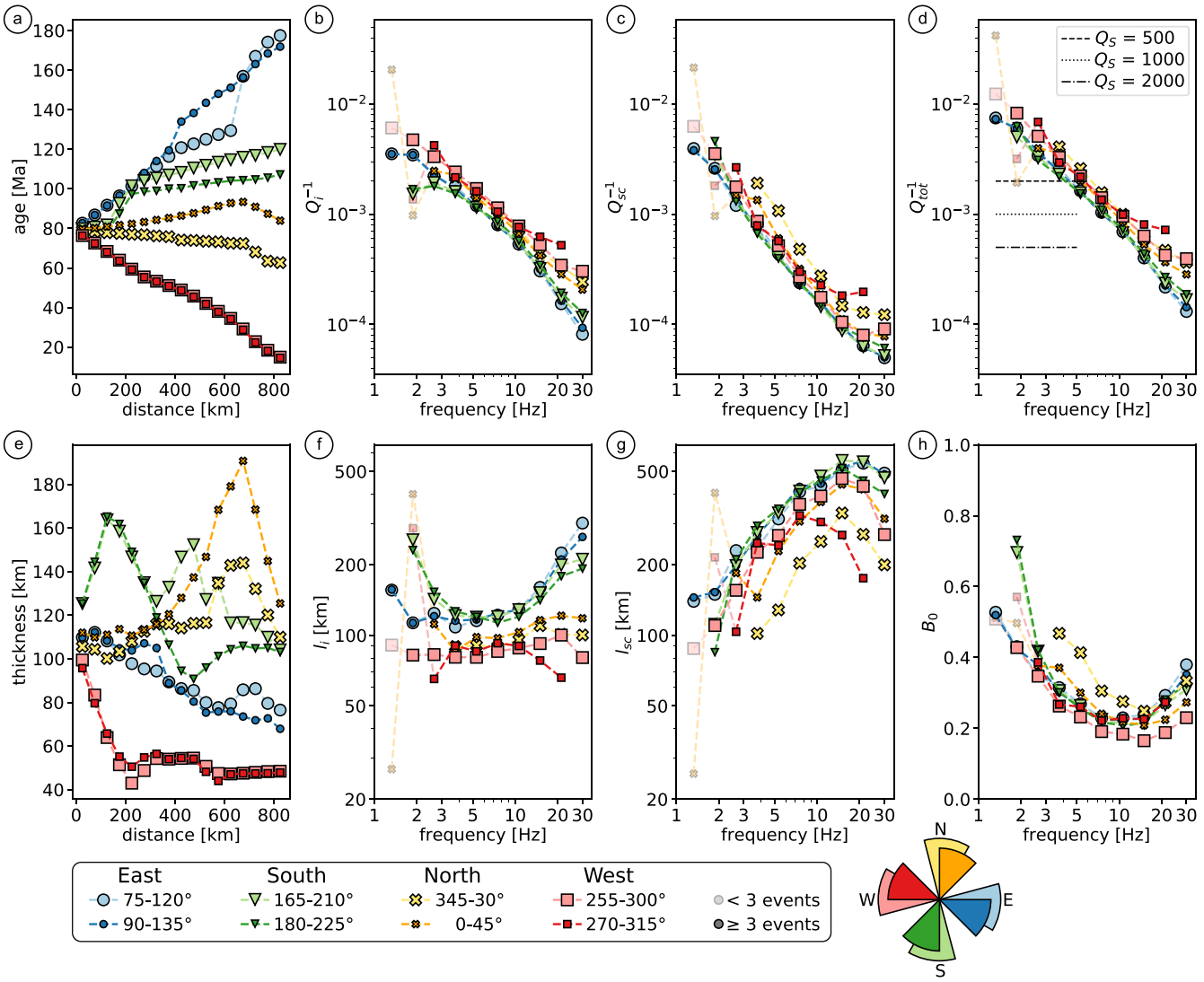

Figure 9. Comparison for (a) age–distance profiles, inverse quality factors for (b) intrinsic attenuation, (c) scattering attenuation and (d) total attenuation including constant Q_S as was used for the oceanic mantle lithosphere with different ages for the numerical modelling of *Po* and *So* waves by Shito *et al.* (2013; $Q_S = 2000$ for 150 Ma) and Shito *et al.* (2015; $Q_S = 500$ for 15 Ma and $Q_S = 1000$ for 30–60 Ma), (e) lithospheric thickness–distance profiles, (f) absorption path length, (g) transport mean free path length and (h) seismic albedo for *So* waves for two azimuthal bins in each direction (east: blue circles, south: green triangles, north: yellow crosses and west: red squares). The rose next to the legend sketches the selected azimuth bins.

the median thickness remains nearly constant. For eastern azimuths, we observe a slight decrease in lithospheric thickness with distance from 110 to 75 km. For northern azimuths, the median lithospheric thickness is constantly at 120 km up to 400–600 km distance and then peaks at 700 km distance with 150–200 km and decreases to 120 km again for larger distances. The lithospheric thicknesses for southern azimuths undulate around 130 km with an amplitude of plus/minus 50 km until it reaches a constant level at 130 km at a distance of 600 km.

The absorption path length l_i (Fig. 9f) is nearly constant between 3 and 10 Hz for all four azimuthal directions and shows an increase for larger frequency. For the western and northern azimuths, l_i is around 80–100 km and slightly increases towards 90–110 km. In the eastern and southern directions, l_i is 120 km in the frequency range between 3 and 10 Hz and increases for lower as well as for higher frequencies.

The transport mean free path length l_{sc} (Fig. 9g) increases from 100–150 to 250–600 km up to a frequency of 10–20 Hz and then decreases again for higher frequencies. For southern and eastern azimuths, the behaviour of the curves are similar and they peak around 600 km at 20 Hz. For northern and western azimuths, the transport mean free path lengths scatter more and are shorter (300–400 km).

The last presented value is the seismic albedo B_0 which indicates the influence of the scattering attenuation on the overall attenuation. As can be seen in Fig. 9(h) for frequencies above 2–3 Hz, the seismic albedo is below or around 0.5 and has a minimum between 0.15–0.3 around 10–20 Hz. For frequencies below 2 Hz, B_0 reaches values above 0.5 and for southern azimuths a value of around 0.7.

5 DISCUSSION

The estimated scattering attenuation coefficients (g_0) between 10^{-4} and 4×10^{-5} m^{-1} are typical for the lithosphere or the upper mantle (Sato *et al.* 2012). This is in line with the suggested propagation mechanism for *So* waves in the lithospheric mantle (Kennett *et al.*

2014). The presented example for the fit of the observed and modelled energies in Fig. 6(a) also demonstrate the shortening of the coda time window in case of a local maximum in the coda for frequencies above 3.54 Hz. This local maximum is probably related to a T-phase arrival. This phase travels mainly in the water column through the Sound Fixing And Ranging (SOFAR) channel with about 1.48 km s^{-1} (Shen 2002). Its arrival might influence the overall shape of the late *So*-wave coda. For our data set, the T-phase might arrive within the chosen coda time window for earthquakes up to an epicentral distance of about 400 km, but Fig. 6(a) shows that the chosen quality criteria are able to avoid including this phase in the inversion. Besides the shortening, we also choose to simultaneously invert events from different distance and we therefore conclude that the presented results are not biased by T-phase arrivals.

For the northern azimuths, the lithospheric thickness increases with age until an azimuth of around 45° and then it slightly decreases. As Kennett *et al.* (2014) showed that a decrease in lithospheric thickness has a similar effect on the resulting wavefield as an increase of the inverse quality factor. For the inverse quality factors, we observe a slight increase from the northwest to the northeast, which is contrary to the expected decrease with age, but the slight reduction in lithospheric thickness for the older ocean ages in the northeast and the before mentioned modelling results of Kennett *et al.* (2014) can explain the observed slightly higher inverse quality factors in the northeast compared to the northwest. In the south, we observe a different pattern. There the thickness decreases with age, which is probably related to a thermal variation. Most likely, this effect is caused by the known hotspots and small-scale upper-mantle upwellings in this region which are associated with Madeira and the Canary Islands (Saki *et al.* 2015; Civiero *et al.* 2021). Therefore, the small undulations in the quality factor and the nearly constant values might be an effect of the trade-off between the age, the thickness and the thermal effect on the attenuation. In western directions, we observe a direct correlation between age and thickness. The peak in the inverse quality factors around 295° corresponds to the thinnest and youngest lithosphere and represents the influence of the mid-oceanic ridge on the attenuation. This observation is inline with the one made by Kennett & Furumura (2013) which also suggested that *Po* and *So* waves are highly attenuated by mid-ocean ridges. The increase of the scattering attenuation towards the southwest (azimuths from 240° to 210° in Fig. 8b) is an indication of the influence of the plate boundary (i.e. the Gloria fault) on the *So* waves. The hypocentres estimated by Krüger *et al.* (2020) indicate that this structure is a deep reaching lithospheric fault. Therefore, the observed behaviour is probably associated with the change in lithospheric thickness and age, as was already suggested by modelling (Kennett *et al.* 2014). For eastern azimuths, the lithospheric thickness decreases with increasing age, which seems to be counter intuitive on a first glance, but is inline with our observations for the south. In contrast to the northeast, we do not observe an increase in attenuation for the thinner lithosphere in the southeast. Probably, the overall influence of the much older and therefore colder lithosphere is greater than the effect of the thermal anomaly on the attenuation which leads to an overall decrease in the quality factors compared to the northeast.

The influence of the ocean age on the quality factors becomes even clearer if we analyse the selected azimuth bins in Fig. 9. We observe a general tendency that the inverse quality factors decrease with the age of the lithospheric plate from the west where the lithosphere is younger to the east where it is older for frequencies above 3 Hz for the intrinsic attenuation and above 10 Hz for the scattering and total attenuation. This implies that the younger the lithosphere the more attenuative it gets at least for frequencies above 3–10 Hz. If we compare our estimates for the total attenuation with Q_S values used by Shito *et al.* (2013, 2015) for modelling *So* waves up to 5 Hz in the Pacific Ocean, we observe that our attenuation estimates are higher. This observation implies that the oceanic lithosphere of the Eastern North Atlantic is probably more attenuative than the one in the Pacific Ocean. We conclude that this is inline with the assumption that due to the slower spreading rate in the Atlantic Ocean the generated *So* wavefield is less stable and not sustainable for long distances and therefore experiences a higher attenuation than in the Pacific Ocean as suggested by Kennett *et al.* (2014). In contrast to the last paragraph, we do not observe a pronounced influence of the lithospheric thickness on the attenuation, but this is most likely related to the fact that the chosen azimuth ranges are not associated with the strong variations in lithospheric thickness and thermal variation in the northeast and southeast which we observe in Fig. 8. Hannemann *et al.* (2016) found that the total crustal thickness below the DOCTAR array is between 4 and 10 km. This is much less than the estimated absorption path length between 60 and 300 km and the transport mean free path length between 100 and 600 km. This size difference implies that the oceanic crust itself has only a weak influence on the appearance of the *So* wave and its coda (Sato *et al.* 2012). Moreover, the absorption path length and the transport mean free path length for older lithospheric ages (eastern and southern azimuth bins) is larger than for younger lithospheric ages (western and northern azimuth bins) which is inline with the former conclusions that the old lithosphere is less attenuative than the young lithosphere. For frequencies above 3 Hz the seismic albedo implies that the scattering attenuation is less or equal to the intrinsic attenuation. Only for southern azimuths and frequencies below 3 Hz the seismic albedo is clearly above 0.5 which indicates that the scattering attenuation dominates the total attenuation. However, if we consider Fig. 9(c), we observe that the scattering attenuation is not remarkably higher for the southern azimuths than for the other directions, but if we take a look at the intrinsic attenuation (Fig. 9b) we observe for the southern azimuths below 3 Hz smaller intrinsic inverse quality factors than for the other directions. This is probably the influence of the plate boundary (i.e. Gloria fault) where a change in ocean age and lithospheric thickness takes place (Figs 7, 8c & d and 9a & e).

6 CONCLUSIONS

In this study, we estimated for the first time intrinsic and scattering attenuation parameters using an envelope inversion of *So*-wave energy of regional events recorded on ocean bottom stations in the Atlantic Ocean and analysed them in comparison with ocean ages and lithospheric thickness. Based on the estimated scattering attenuation coefficients (10^{-4} $m^{-1} \leq g_0 \leq 4 \times 10^{-5}$ m^{-1}) which show typical values for the lithosphere and upper mantle (Sato *et al.* 2012), we confirm that the *So* waves mainly propagate through the oceanic mantle lithosphere as was proposed by numerical modelling (Kennett & Furumura 2013). Furthermore, the comparison with attenuation parameters used for the modelling of *So* waves in the Pacific Ocean indicates that the oceanic lithosphere of the Atlantic Ocean is more attenuative ($Q_s < 500$ for frequencies below 5 Hz) than the one of the Pacific Ocean. In a detailed analysis, we concluded that the estimated attenuation parameters can be explained by a rather complex interplay between lithospheric thickness, ocean age and thermal effects. The influence of the mid-ocean ridge towards the west is clearly visible in an increase of the estimated

inverse quality factors. The effect of the hotspots and small-scale upper-mantle upwellings in the southeast of the ocean bottom stations (Saki *et al.* 2015; Civiero *et al.* 2021) together with the old lithospheric ages lead to nearly constant inverse quality factors for a wider azimuthal range. However, for future studies, including heat flow measurements or geodynamic models of lithospheric temperature will probably allow to draw further conclusions on the influence of thermal variations on attenuation. For this study, by concentrating on specific azimuth ranges which represent the youngest and oldest parts, and those azimuth ranges which showed the least variation in age, we draw three main conclusions. First, an increase in attenuation can be observed for a decrease in lithospheric age which is inline with previous observations made in the Pacific Ocean by Kennett *et al.* (2014) and Shito *et al.* (2013, 2015). Second, for frequencies above 3 Hz the scattering attenuation is less or equal to the intrinsic attenuation. However, for southern azimuths and frequencies below 3 Hz we estimated a clear reduction in intrinsic attenuation leading to a dominance of scattering attenuation. This effect is most likely related to the influence of the Gloria fault, that is the plate boundary towards the south. Third, the estimated absorption and transport mean free path lengths between 60 and 600 km indicate only a weak influence of the oceanic crust on the appearance of the *So* wave and its coda (Sato *et al.* 2012).

In summary, this study shows that the analysis of *So* waves of local and regional earthquakes at OBSs provides insight into the attenuation parameters of the surrounding lithosphere. Furthermore, a combined analysis with lithospheric ages and thicknesses is helpful to draw further conclusion on the thermal state of the lithosphere in specific azimuthal ranges.

ACKNOWLEDGEMENTS

We have used open source software and would like to gratefully acknowledge: GIMP; Inkscape; GMT—The Generic Mapping Tools developed by Paul Wessel and Walter H. F. Smith (Wessel *et al.* 2013); ObsPy (Beyreuther *et al.* 2010) and Qopen (Eulenfeld & Wegler 2016). We greatly acknowledge the DEPAS instrument pool for allocation of the OBS stations, the University of Hamburg for allocating ship time and the great help of the Poseidon crew during deployment and recovery of the OBS stations (RV Poseidon cruises POS416 and POS431). The DOCTAR project was funded by the DFG (Deutsche Forschungsgemeinschaft/German Research Foundation KR1935/13 and DA478/21-1). We thank Joshua Russell and an anonymous reviewer for their helpful comments during the review process which further improved the manuscript.

DATA AVAILABILITY

The sea floor seismological data were archived by Alfred Wegener Institute (AWI), Helmholtz Centre for Polar Research, Bremerhaven, Germany, and are available upon request.

REFERENCES

Aki, K. & Richards, P.G., 2002. *Quantitative Seismology,* 2nd edn, University Science Books.

Alfred-Wegener-Institut Helmholtz-Zentrum für Polar- und Meeresforschung *et al*, 2017. DEPAS (Deutscher Geräte-Pool für amphibische Seismologie): German instrument pool for amphibian seismology, *J. Largescale Res. Facil.,* **3,** A122, doi:10.17815/jlsrf-3-165.

Beyreuther, M., Barsch, R., Krischer, L., Megies, T., Behr, Y. & Wassermann, J., 2010. ObsPy: a Python toolbox for seismology, *Seismol. Res. Lett.,* **81**(3), 530–533.

Bird, P., 2003. An updated digital model of plate boundaries, *Geochem. Geophys. Geosyst.,* **4**(3), doi:10.1029/2001GC000252.

Civiero, C., Custódio, S., Neres, M., Schlaphorst, D., Mata, J. & Silveira, G., 2021. The role of the seismically slow Central-East Atlantic Anomaly in the genesis of the Canary and Madeira volcanic provinces, *Geophys. Res. Lett.,* **48,** e2021GL092874.

Dziewonski, A.M. & Anderson, D.L., 1981. Preliminary reference Earth model, *Phys. Earth planet. Inter.,* **25**(4), 297–356.

Emoto, K., Sato, H. & Nishimura, T., 2010. Synthesis of vector wave envelopes on the free surface of a random medium for the vertical incidence of a plane wavelet based on the Markov approximation, *J. geophys. Res.,* **115,** 1–15.

Eulenfeld, T. & Wegler, U., 2016. Measurement of intrinsic and scattering attenuation of shear waves in two sedimentary basins and comparison to crystalline sites in Germany, *Geophys. J. Int.,* **205**(2), 744–757.

GEBCO Compilation Group, 2020. GEBCO 2020 Grid, doi:10.5285/a29c5465-b138-234d-e053-6c86abc040b9.

Hannemann, K., Krüger, F. & Dahm, T., 2014. Measuring of clock drift rates and static time offsets of ocean bottom stations by means of ambient noise, *Geophys. J. Int.,* **196**(2), 1034–1042.

Hannemann, K., Krüger, F., Dahm, T. & Lange, D., 2016. Oceanic lithospheric *S*-wave velocities from the analysis of *P*-wave polarization at the ocean floor, *Geophys. J. Int.,* **207,** 1796–1817.

Hannemann, K., Krüger, F., Dahm, T. & Lange, D., 2017. Structure of the oceanic crust and upper mantle north of the Gloria Fault in the eastern mid-Atlantic by receiver function analysis, *J. geophys. Res.,* **122**(10), 7927–7950.

Jackson, I., 2007. 2.17: Properties of rocks and minerals: physical origins of anelasticity and attenuation in rock, in *Treatise on Geophysics,* Vol. 2, pp. 493–525, ed. Schubert, G., Elsevier.

Kennett, B.L.N. & Furumura, T., 2013. High-frequency *Po*/*So* guided waves in the oceanic lithosphere: I–long distance propagation, *Geophys. J. Int.,* **195,** 1862–1877.

Kennett, B.L.N., Furumura, T. & Zhao, Y., 2014. High-frequency *Po*/*So* guided waves in the oceanic lithosphere: II–heterogeneity and attenuation, *Geophys. J. Int.,* **199,** 614–630.

Krüger, F., Dahm, T. & Hannemann, K., 2020. Mapping of Eastern North Atlantic Ocean seismicity from *Po*/*So* observations at a mid-aperture seismological broad-band deep sea array, *Geophys. J. Int.,* **221**(2), 1055–1080.

Müller, R.D., Sdrolias, M., Gaina, C. & Roest, W.R., 2008. Age, spreading rates, and spreading asymmetry of the world's ocean crust, *Geochem. Geophys. Geosyst.,* **9**(4), doi:10.1029/2007GC001743.

Paasschens, J. C. J., 1997. Solution of the time-dependent Boltzmann equation, *Phys. Rev. E,* **56**(1), 1135–1141.

Pasyanos, M.E., Masters, T.G., Laske, G. & Ma, Z., 2014. LITHO1.0: an updated crust and lithospheric model of the Earth, *J. geophys. Res.,* **119,** 2153–2173.

Saki, M., Thomas, C., Nippress, S.E. & Lessing, S., 2015. Topography of upper mantle seismic discontinuities beneath the North Atlantic: the Azores, Canary and Cape Verde plumes, *Earth planet. Sci. Lett.,* **409,** 193–202.

Sato, H., Fehler, M.C. & Maeda, T., 2012. *Seismic Wave Propagation and Scattering in the Heterogeneous Earth,* 2nd edn, Springer.

Shen, Y., 2002. Seismicity at the southern East Pacific Rise from recordings of an ocean bottom seismometer array, *J. geophys. Res.,* **107**(B12), 2368.

Shito, A., Suetsugu, D., Furumura, T., Sugioka, H. & Ito, A., 2013. Small-scale heterogeneities in the oceanic lithosphere inferred from guided waves, *Geophys. Res. Lett.,* **40,** 1708–1712.

Shito, A., Suetsugu, D. & Furumura, T., 2015. Evolution of the oceanic lithosphere inferred from *Po*/*So* waves traveling in the Philippine Sea Plate, *J. geophys. Res.,* **120,** 5238–5248.

Stähler, S.C. *et al.*, 2016. Preliminary performance report of the RHUM-RUM ocean bottom seismometer network around La Réunion, western Indian Ocean, *Adv. Geosci.,* **41,** 43–63.

Vilanova, S.P., Nunes, C.F. & Fonseca, J.F.B.D., 2003. Lisbon 1755: a case of triggered onshore rupture?, *Bull. seism. Soc. Am.,* **93**(5), 2056–2068.

Walker, D.A. & Sutton, G.H., 1971. Oceanic mantle phases recorded on hydrophones in the Northwestern Pacific at distances between 9° and 40°, *Bull. seism. Soc. Am.,* **61**(1), 65–78.

Wessel, P., Smith, W.H.F., Scharroo, R., Luis, J. & Wobbe, F., 2013. Generic Mapping Tools: improved version released, *EOS, Trans. Am. geophys. Un.,* **94**(45), 409–410.

Zoeppritz, K., 1919. Über Erdbebenwellen Part VII b. Über Reflexion und Durchgang seismischer Wellen durch Unstetigkeitsflaechen, *Nachr. Ges. Wiss. Gött.,* **1919,** 66–84.

APPENDIX: AMPLIFICATION OF *SV* WAVES AT THE OCEAN BOTTOM

If an *SV* wave arrives at the interface between the water column and the ocean bottom, three waves are generated at the interface: a reflected *SV* wave and a reflected *P* wave in the ocean bottom, and a refracted *P* wave in the water column (Fig. A1). In order to estimate the amplification which will be measured at the interface for an incident *SV* wave, we need to consider the displacements due to the incident *SV* wave, the reflected *SV* wave and the reflected *P* wave (similar as in the case of an incident *P* wave, see Hannemann *et al.* 2016). Therefore, we need to calculate both reflection coefficients for the ocean bottom. We follow the notation by Aki & Richards (2002) who used an acute accent to represent an upgoing wave (e.g. $\acute{S}$) and a grave accent to represent a downgoing wave (e.g. $\grave{S}$). We calculated the coefficients $\acute{S}\grave{S}$ and $\acute{S}\grave{P}$:

$$\acute{S}\grave{S} = -\frac{1-k(1-l)}{1+k(1+l)}, \tag{A1}$$

$$\acute{S}\grave{P} = -\frac{\rho_1 v_{s1}\,\cos\varphi_{p2}\,\sin(4\,\varphi_{s0})}{\rho_2 v_{p2}\,\cos\varphi_{p1}}\,\frac{1}{1+k(1+l)}, \tag{A2}$$

with

$$k = \left(\tfrac{v_s}{v_{p2}}\right)^2 \tfrac{\rho_1}{\rho_2}\sin(2\varphi_{s0})\sin\left(2\varphi_{p2}\right), \tag{A3}$$

$$l = \left(\frac{v_{p1}}{v_s}\right)^2 \frac{\cos(2\varphi_{s0})}{\sin\left(2\varphi_{p1}\right)\tan(2\varphi_{s0})}. \tag{A4}$$

These coefficients are similar to the ones published by Zoeppritz (1919) except for the opposite sign in eq. (A2) which results from an opposite definition of the polarization direction of the reflected *P* wave.

The resulting amplitude of the vertical displacement is found by considering the displacements of all wave types in the ocean bottom in *z*-direction (compare Fig. A1) and inserting eqs (A1)–(A4):

$$A_z^s = \left(\acute{S}\grave{S}+1\right)\sin\varphi_{s0} - \acute{S}\grave{P}\cos\varphi_{p1}, \tag{A5}$$

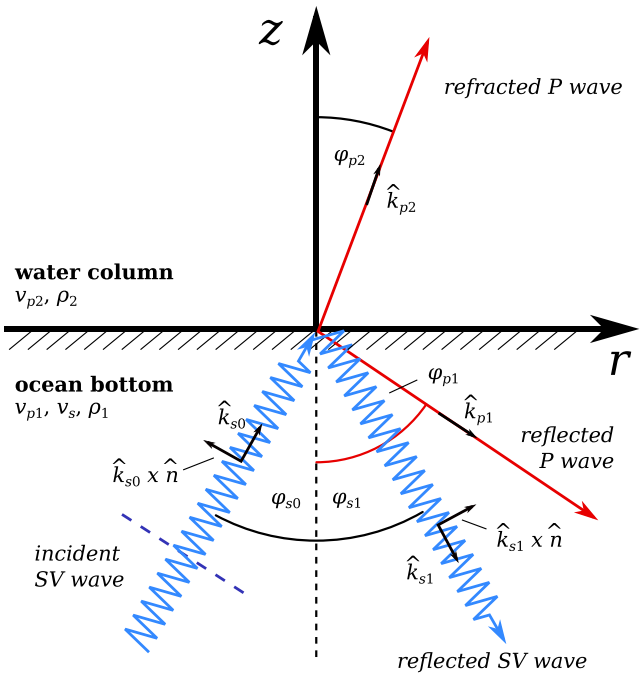

Figure A1. *SV* waves (blue) and *P* waves (red) at the interface between water column and ocean bottom resulting from an incoming *SV* wave front (represented as dashed blue line). The direction of particle motions of the single wave types are shown as small black arrows. The normal of the *zr*-plane $\hat{n}$ points into the negative transverse direction. The ocean bottom has the *P*-wave velocity v_{p1}, the *S*-wave velocity v_s and the density ρ_1. The water column has the *P*-wave velocity v_{p2} and the density ρ_2.

$$A_z^s = \left(-\frac{1-k(1-l)}{1+k(1+l)}+1\right)\sin\varphi_{s0} + \frac{\cos\varphi_{p2}\,\sin(4\,\varphi_{s0})\,\rho_1 v_{s1}}{\cos\varphi_{p1}\rho_2 v_{p2}}\,\frac{\cos\varphi_{p1}}{1+k(1+l)}, \tag{A6}$$

$$A_z^s = \frac{2\,k\rho_2 v_{p2}\,\sin\varphi_{s0}\,\cos\varphi_{p1} + \cos\varphi_{p2}\,\sin(4\,\varphi_{s0})\,\rho_1 v_{s1}\,\cos\varphi_{p1}}{\cos\varphi_{p1}\rho_2 v_{p2}\,[1+k(1+l)]}, \tag{A7}$$

$$A_z^s = \frac{2\,\rho_1 v_s\,\sin(2\,\varphi_{s0})\,\cos\varphi_{p2}\,\cos\varphi_{p1}}{\rho_2 v_{p2}\cos\varphi_{p1} + \rho_1\cos\varphi_{p2}\left[4\,v_s\,\sin^2\varphi_{s0}\,\cos\varphi_{s0}\,\cos\varphi_{p1} + v_{p1}\cos^2(2\,\varphi_{s0})\right]}. \tag{A8}$$

The resulting amplitude of horizontal displacement is found by considering the displacements of all wave types in the ocean bottom in *r*-direction (compare Fig. A1) and inserting eqs (A1)–(A4):

$$A_r^s = \left(\grave{S}\grave{S} - 1\right)\cos\varphi_{s0} + \grave{S}\grave{P}\sin\varphi_{p1}, \tag{A9}$$

$$A_r^s = \left(-\frac{1-k(1-l)}{1+k(1+l)}-1\right)\cos\varphi_{s0} - \frac{\cos\varphi_{p2}\sin(4\varphi_{s0})\,\rho_1 v_{s1}}{\cos\varphi_{p1}\rho_2 v_{p2}}\,\frac{\sin\varphi_{p1}}{1+k(1+l)}, \tag{A10}$$

$$A_r^s = \frac{-2\,(1+kl)\cos\varphi_{s0}\cos\varphi_{p1}\rho_2 v_{p2} - \cos\varphi_{p2}\sin(4\varphi_{s0})\,\rho_1 v_{s1}\sin\varphi_{p1}}{\cos\varphi_{p1}\rho_2 v_{p2}\,[1+k(1+l)]}, \tag{A11}$$

$$A_r^s = \frac{-2\cos\varphi_{s0}\left(\rho_1 v_{p1}\cos(2\varphi_{s0})\cos\varphi_{p2} + \rho_2 v_{p2}\cos\varphi_{p1}\right)}{\rho_2 v_{p2}\cos\varphi_{p1} + \rho_1\cos\varphi_{p2}\left[4v_s\sin^2\varphi_{s0}\cos\varphi_{s0}\cos\varphi_{p1} + v_{p1}\cos^2(2\varphi_{s0})\right]}. \tag{A12}$$